Image Cover Sheet

CLASSIFICATION	SYSTEM NUMBER 514630
UNCLASSIFIED	

TITLE

Impedance-Matched Absorbers for Finite-Difference Parabolic Equation Algorithms

System Number:

Patron Number:

Requester:

Notes:

DSIS Use only:

Deliver to: CL

Impedance-matched absorbers for finite-difference parabolic equation algorithms

David Yevick
Department of Physics, University of Waterloo, 200 University Avenue West, Waterloo, Ontario N2L 3G1, Canada

David J. Thomson
Defence Research Establishment Atlantic, P.O. Box 1012, Dartmouth, Nova Scotia B2Y 3Z7, Canada

(Received 25 November 1998; revised 22 November 1999; accepted 11 December 1999)

In this paper, a perfectly matched layer (PML) absorber, recently introduced into the electromagnetic propagation literature by Bérenger [J. Comput. Phys. **114**, 185–200 (1994)], is adapted for use with both paraxial and wide-angle acoustic parabolic equations (PEs). Our procedure incorporates an imaginary component into the transverse coordinate that mimics the introduction of a fictitious absorber on the edge of the computational grid. Use of such an impedance-matched layer can significantly reduce spurious reflections compared to physical absorbing layer methods and thus allows a smaller number of boundary points to be employed in PE calculations. Numerical results obtained with several higher-order propagator approximations confirm that such impedance-matched absorbers efficiently eliminate reflections.
[S0001-4966(00)04703-2]

PACS numbers: 43.30.Bp [SAC-B]

INTRODUCTION

Several one-way propagation procedures currently exist for solving various parabolic equations relevant to underwater acoustics (see Ref. 1, pp. 343–412 and the references therein). In particular, numerical methods have been developed to treat both range-independent and range-dependent inelastic and elastic media that accurately account for discontinuous changes in material properties, highly divergent fields and bidirectional field propagation.[2] Each parabolic equation must be supplemented with relevant boundary conditions along the cross-range edges of the computational grid. For underwater sound propagation, the ocean surface is usually modeled simply as a pressure-release boundary. A more complicated procedure is required, however, to treat the interaction of the field beneath a penetrable sea-bottom where a downgoing radiation condition usually applies.

In treating radiation conditions, two cases can be distinguished. The first of these results if the field physically undergoes further reflection at the position of the computational window boundary or at some distance beyond this location. Sometimes, the boundary interaction can be described in terms of a local impedance condition as in radar[3] and atmospheric sound[4] propagation near the Earth's surface. In underwater acoustics, however, such locally reacting conditions are generally not applicable, and nonlocal boundary conditions that incorporate the full spectral behavior of the reflection coefficient describing the interaction with the subbottom must be used instead.[5]

A second case results if the subbottom is assumed to be homogeneous and semi-infinite so that all power leaving the computational domain should physically radiate downward to infinity. Numerous local and nonlocal boundary conditions of varying degrees of accuracy may then be applied to remove this component of the acoustic field. The most direct procedure is to introduce a physical absorbing layer which, if the absorber strength increases sufficiently gradually, removes a large fraction of the incident field by an attenuation mechanism without introducing spurious reflections.[6–12] Generally, the absorber is terminated by imposing a pressure-release condition at the base of the layer. For some problems, the use of physical absorbers necessitates a large number of grid points, and can be computationally inefficient. Consequently, several alternate approaches for handling the downgoing radiation field have been proposed. The most accurate of these involve nonlocal procedures that employ the previous history of the acoustic field along the computational window edges to determine the downgoing boundary condition at the successive propagation step.[5,13–19] While such nonlocal methods can be made arbitrarily precise,[20] their implementation requires more effort compared to local methods. Moreover, they cannot easily be adapted to three-dimensional problems or extended to accommodate multiterm Padé[21] or split-step Padé PEs.[22]

Recently, several researchers have examined an alternative absorbing mechanism that is equivalent to introducing a fictitious imaginary component into the transverse coordinates. Such a procedure greatly reduces any unphysical (and unwanted) reflections from the boundary layer.[23–33] Although this observation had its roots in early analytic work on electromagnetic modes,[23] its first major application was in the area of finite-difference time-domain analysis of electromagnetic fields.[24] A considerable amount of work has since been expended on developing a theoretical basis for the method and on applying this knowledge to the generation of increasingly accurate radiation boundary conditions. The formalism has since been adapted to one-way wave propagation by several authors,[34,35] as well as to elastic fields.[36] Careful analyses of the errors arising from grid-point discretization

have been performed and compared to numerical results.[32,37,38]

In this paper, we address a key element that extends previous work[38] on this so-called perfectly matched layer (PML) method, especially as it relates to frequency-domain propagation in underwater acoustics. Namely, we perform a detailed numerical study of the manner in which the reflectivity of such layers depends on the wide-angle capability of the underlying propagation technique. Our results indicate that in fact the reflection coefficient is almost unchanged with the wide-angle order of the propagation method, from which we conclude that the detailed theory that has been derived for paraxial methods should apply as well to higher-order wide-angle techniques.

I. PE PROPAGATORS

As a first step, we construct several one-way propagation equations for a medium with a varying density $\rho(z)$ located between the surface ($z=0$) and bottom ($z=z_b$) of a stratified ocean. The sound speed and absorption are designated by $c(z)$ and $\alpha(z)$, respectively. Defining a reference wave number $k_0=\omega/c_0$, we relate the field ψ to the complex pressure p according to

$$p(r,z)=\frac{\psi(r,z)\exp(ik_0r)}{\sqrt{k_0r}}. \tag{1}$$

In terms of the square-root operator $\sqrt{1+X}$, which is composed of the dimensionless expression

$$X=N^2-1+k_0^{-2}\rho\frac{\partial}{\partial z}\left(\rho^{-1}\frac{\partial}{\partial z}\right), \tag{2}$$

with $N(z)=n(z)[1+i\alpha(z)]$ and $n(z)=c_0/c(z)$, outgoing propagating waves in the far-field ($k_0r\gg1$) can be described formally by the exact "one-way" evolution equation[7–9]

$$\frac{\partial\psi}{\partial r}=ik_0\{-1+\sqrt{1+X}\}\psi. \tag{3}$$

The propagation operator associated with this equation is

$$\psi(r+\Delta r,z)=\exp\{-\delta+\delta\sqrt{1+X}\}\psi(r,z), \tag{4}$$

where we have set $\delta=ik_0\Delta r$. Combined with appropriate boundary conditions, Eq. (4) yields the exact solution of the discretized one-way propagation problem.

The standard, paraxial PE results if the square-root operator in Eq. (3) is approximated by

$$-1+\sqrt{1+X}\approx\tfrac{1}{2}X. \tag{5}$$

Substituting Eq. (5) into Eq. (3) yields

$$\frac{\partial\psi}{\partial r}=\tfrac{1}{2}ik_0X\psi, \tag{6}$$

with the associated one-way propagator

$$\psi(r+\Delta r,z)=\exp\{\tfrac{1}{2}\delta X\}\psi(r,z). \tag{7}$$

The accuracy of the paraxial equation is limited to acoustic waves whose dominant horizontal wave numbers lie close to the value chosen for k_0. Sound energy emitted from more highly divergent radiation sources is more accurately described by wide-angle equations. Two procedures are commonly employed to construct energy-conserving wide-angle equations and propagators from Eq. (3) and Eq. (7).

In the first procedure, a $[M,M]$-Padé approximation is applied to $\sqrt{1+X}$ followed by M $[1,1]$-Padé approximants with respect to δ. That is, first write[21]

$$\psi(r+\Delta r,z)=\exp\left\{\sum_{m=1}^{M}\frac{\delta a_{m,M}X}{1+b_{m,M}X}\right\}\psi(r,z), \tag{8}$$

where the real coefficients $a_{m,M}$ and $b_{m,M}$ are given by

$$a_{m,M}=\frac{2}{2M+1}\sin^2\frac{m\pi}{2M+1}, \tag{9}$$

$$b_{m,M}=\cos^2\frac{m\pi}{2M+1}, \tag{10}$$

followed by the unitary single-term approximations

$$\exp\frac{\delta a_{m,M}X}{1+b_{m,M}X}\approx\frac{1+c^{+}_{m,M}X}{1+c^{-}_{m,M}X}, \tag{11}$$

with $c^{\pm}_{m,M}=b_{m,M}\pm\frac{1}{2}\delta a_{m,M}$.

The lowest-order ($M=1$) equation of this series gives $a_{1,1}=1/2$ and $b_{1,1}=1/4$ and leads to the rational-linear approximation

$$-1+\sqrt{1+X}\approx\frac{\frac{1}{2}X}{1+\frac{1}{4}X}. \tag{12}$$

The resulting third-order PE,

$$\left(1+\frac{1}{4}X\right)\frac{\partial\psi}{\partial r}=\frac{1}{2}ik_0X\psi, \tag{13}$$

is due to Claerbout[39] and can be put in the implicit finite-difference form

$$\{1+\tfrac{1}{4}(1-\delta X)\}\psi(r+\Delta r,z)=\{1+\tfrac{1}{4}(1+\delta X)\}\psi(r,z). \tag{14}$$

It should be noted that although a higher-order Padé approximant to the propagator will generally allow larger range steps to be taken, the accuracy of the overall approximation with respect to X will not be improved.

Once Eq. (8) has been evaluated to the desired (transverse) Padé order in X, the exponential of the sum of commuting terms may be written as the product of exponentials of the individual terms and a $[1,1]$-Padé approximant can then be applied to each of these partial propagators. Alternatively, a $[M,M]$-Padé approximation may be applied to the exponential of the full sum and the numerator and denominator of the resulting expression factored into the products of first-order polynomial expressions in X. In either case, once δ is specified, the algebraic expressions for the propagator can be recast numerically into the partial fraction form

$$\exp\{-\delta+\delta\sqrt{1+X}\}=1+\sum_{m=1}^{M}\frac{\tilde{a}_{m,M}X}{1+\tilde{b}_{m,M}X}. \tag{15}$$

Consequently, in a multiprocessing system, each processor can be assigned one of the terms, $m=1,\ldots,M$ on the right-hand side of the expression

$$\psi(r+\Delta r,z)=\psi(r,z)+\sum_{m=1}^{M}\frac{\tilde{a}_{m,M}X}{1+\tilde{b}_{m,M}X}\psi(r,z), \tag{16}$$

so that all M terms may be evaluated in parallel and then summed. In two dimensions, all of the above procedures involve numerically efficient routines for multiplying and inverting tridiagonal matrices and have therefore been widely applied.

Due to the use of [1,1]-Padé approximants with respect to δ, however, the above procedure requires sufficiently small values of δ in order to maintain accuracy. We therefore consider a second procedure which permits larger values of δ for a desired level of accuracy.[22] In particular, we apply a $[M,M]$-Padé approximation with respect to X directly to the exact exponential propagation operator to generate an expression of the form

$$\exp\{-\delta+\delta\sqrt{1+X}\}=\frac{1+G_M(\delta,X)}{1+G_M^*(\delta,X)}, \tag{17}$$

where * denotes complex conjugate. In the $M=2$ case, for example, we find G_2 given by

$$G_2(\delta,X)=\frac{g_{2,1}(\delta)X+g_{2,2}(\delta)X^2}{g_2(\delta)}, \tag{18}$$

with

$$g_2(\delta)=\delta^2-3, \tag{19}$$

$$g_{2,1}(\delta)=\tfrac{1}{4}\delta^3+\tfrac{1}{2}\delta^2-\tfrac{3}{4}\delta-\tfrac{9}{4}, \tag{20}$$

$$g_{2,2}(\delta)=\tfrac{1}{48}\delta^4+\tfrac{1}{16}\delta^3-\tfrac{1}{16}\delta^2-\tfrac{27}{16}\delta-\tfrac{27}{16}. \tag{21}$$

The corresponding $M=3$ propagator is derived from

$$G_3(\delta,X)=\frac{g_{3,1}(\delta)X+g_{3,2}(\delta)X^2+g_{3,3}(\delta)X^3}{g_3(\delta)}, \tag{22}$$

in which

$$g_3(\delta)=\delta^6-18\delta^4+135\delta^2-135, \tag{23}$$

$$g_{3,1}(\delta)=\tfrac{1}{4}\delta^7+\tfrac{3}{4}\delta^6-\tfrac{9}{2}\delta^5-\tfrac{33}{2}\delta^4+\tfrac{135}{4}\delta^3+\tfrac{585}{4}\delta^2-\tfrac{135}{4}\delta-\tfrac{675}{4}, \tag{24}$$

$$g_{3,2}(\delta)=\tfrac{1}{40}\delta^8+\tfrac{1}{8}\delta^7-\tfrac{3}{8}\delta^6-3\delta^5+\tfrac{3}{4}\delta^4+\tfrac{225}{8}\delta^3+\tfrac{225}{8}\delta^2-\tfrac{135}{4}\delta-\tfrac{405}{8}, \tag{25}$$

$$g_{3,3}(\delta)=\tfrac{1}{960}\delta^9+\tfrac{1}{160}\delta^8-\tfrac{1}{64}\delta^7-\tfrac{11}{64}\delta^6-\tfrac{3}{64}\delta^5+\tfrac{57}{32}\delta^4+\tfrac{45}{16}\delta^3-\tfrac{135}{64}\delta^2-\tfrac{405}{64}\delta-\tfrac{135}{64}. \tag{26}$$

For $M=2$ and $M=3$, respectively, these results are equivalent to applying a $[M,M]$-Padé approximation to the square-root operator followed by a $[M,M]$-Padé approximation to the resulting exponential function. This equivalence holds for any M. Since propagator approximations for $M>3$ are tedious to express analytically, however, it is expedient to compute them numerically once δ is specified.

II. ABSORBING LAYERS

A central problem encountered when underwater acoustic fields are propagated numerically is that of removing downward radiating field components at the computational boundary. In this section, we analyze two procedures for attenuating radiated energy that are based on using a physical absorbing layer and a perfectly matched layer, respectively. We first consider the standard parabolic equation and apply the half-range Fourier transform

$$\Psi(s,z)=\int_0^\infty \psi(r,z)\exp(-isr)dr \tag{27}$$

to Eq. (6) to obtain

$$\frac{\partial^2\Psi}{\partial z^2}+\gamma^2(s)\Psi=0, \tag{28}$$

where $\gamma^2(s)=k_0^2(N^2-1-2s/k_0)$ is the squared vertical wave number and we have chosen the branch $\Im\gamma>0$. The horizontal wave number s of the standard PE is related to the horizontal wave number k of the scalar wave equation by the mapping $k=k_0\sqrt{1+2s/k_0}$ (see, e.g., Ref. 15).

Consider a uniform layer of thickness h appended to the base $z=z_b$ of the PE computational domain. Within a thin homogeneous layer just above $z=z_b$, the solution to Eq. (28) can be written as

$$\Psi_-=\exp[i\gamma_-|z-z_b|]+R\exp[-i\gamma_-|z-z_b|]. \tag{29}$$

Here, the subscripts "$\pm$" are used to denote quantities at $z=z_b\pm 0$, R is the plane wave reflection coefficient, and the dependence on s has been suppressed. In $z_b<z<z_b+h$, we set $\rho_+=\rho_-$, $n_+=n_-$ and impose a Dirichlet boundary condition on the field at $z=z_b+h$.

In the case of a physical absorber, we set $N_+=n_+(1+i\alpha_+)$ and obtain for the field in the layer

$$\Psi_+=T\exp[i\gamma_+(z-z_b)]-T\exp[-i\gamma_+(z-z_b-2h)]. \tag{30}$$

Imposing the continuity of Ψ and $\rho^{-1}\Psi_z$ across $z=z_b$ then yields the reflection coefficient of the physical absorbing layer in the form

$$R=\frac{R_0-\exp(2i\gamma_-h)}{1-R_0\exp(2i\gamma_-h)}=R_0+(R_0^2-1)\exp(2i\gamma_-h)+\ldots, \tag{31}$$

where $R_0=(\gamma_--\gamma_+)/(\gamma_-+\gamma_+)$ is the reflection coefficient associated with the top of the layer. The second term in Eq. (31) corresponds to the amplitude reduction due to a round-trip passage of the wave in the lossy layer. The apparent reflection loss of this wave component is given by

$$R\approx\exp(2i\gamma_-h)\Rightarrow|R|\approx\exp(-2\Im\gamma_-h). \tag{32}$$

Clearly, the jump in absorption across $z=z_b$ must be small to keep $|R_0|$ small. However, in order to significantly attenuate the round-trip component of the reflected field, smaller values of α_+ must be compensated by larger values of h. An acceptable trade-off between these requirements can be realized by smoothly tapering the absorber strength $\alpha(z)$ within

the layer. This can render $R_0 \approx 0$ for a given maximum value of α without changing h.[6-12]

In a perfectly matched layer, we instead set the refractive index $N_+ = N_-$ (so that $\gamma_+ = \gamma_-$) and stretch the z-coordinate for $z_b < z < z_b + h$ according to $z^* = z(1+ia)$. Accordingly, inserting

$$\frac{\partial}{\partial z} \rightarrow \frac{\partial}{\partial z^*} = (1+ia)^{-1} \frac{\partial}{\partial z} \tag{33}$$

in Eq. (28), transforms the standard PE for $\Psi^*(z) = \Psi(z^*)$ in the layer into

$$(1+ia)^{-2} \frac{\partial^2 \Psi^*}{\partial z^2} + \gamma_+^2(s)\Psi^* = 0. \tag{34}$$

Proceeding as in the case of the physical absorber, we find that the field just above $z = z_b$ still has the form of Eq. (29), while inside the layer the solution that satisfies a pressure-release condition at the stretched depth $z^* = z_b + h^*$ can be written as

$$\Psi_+^* = T \exp[i\gamma_+(z^* - z_b)] - T \exp[-i\gamma_+(z^* - z_b - 2h^*)]. \tag{35}$$

For constant a, the continuity conditions across $z = z_b$ become $\Psi_- = \Psi_+^*$ and $\partial_z \Psi_- = (1+ia)^{-1} \partial_z \Psi_+^*$. Applying these conditions to Eq. (29) and Eq. (35) yields the result

$$R = -\exp[2i\gamma_+ h^*] \Rightarrow |R| = \exp[-2(a\Re\gamma_+ + \Im\gamma_+)h]. \tag{36}$$

Note that $\Im\gamma_+ > 0 \Rightarrow \Re\gamma_+ > 0$. The formula for R in Eq. (36) corresponds to the expression obtained by Bérenger in an electromagnetic context.[24] It exhibits the remarkable feature that a reflected wave from the top of the PML layer is absent.

While increasing the value of α_+ in Eq. (32) yields unacceptably large values of $|R_0|$, this restriction does not appear to apply to a in Eq. (36). This attractive PML property for continuous media does not hold true, however, when the continuous problem is discretized on a computational grid.[37,38] In this case, the use of a suitably tapered profile $a(z)$ can significantly reduce the discretization-induced reflections. For this purpose, we choose for $0 < z - z_b < h$ an $a(z)$-profile of the form[37]

$$a(z) = \tfrac{1}{2} p\{1 - \cos[(z - z_b)\pi/h]\}^q \equiv H(p,q) \tag{37}$$

in our subsequent finite-difference calculations incorporating perfectly matched layer absorbers.

Within the absorbing layer, the numerical implementation of the loss mechanisms differ for the two procedures. This is seen by inspection of the standard PE of Eq. (6), which we write as

$$\frac{\partial \psi}{\partial r} = \underbrace{\frac{1}{2} ik_0(N^2 - 1)\psi}_{\text{lens}} + \underbrace{\frac{1}{2}(i/k_0)\frac{\partial^2 \psi}{\partial z^2}}_{\text{diffraction}}. \tag{38}$$

For the physical absorber, the introduction of loss into the refractive index affects the coefficient of ψ in the lens term. In contrast, for the perfectly matched layer, the introduction of a stretched depth coordinate z^* affects the computation of the Laplacian in the diffraction term.

The above analysis for the standard PE also applies to the higher-order PEs of Eq. (15). These equations only differ from the paraxial equation in the form of the expression for the vertical wave number associated with a given PE approximation, which only affects the PE dispersion relation. That is, the squared vertical wave number for the Mth-order Padé approximation given in Eq. (15) is given by[40]

$$\gamma_M^2 = k_0^2\{N^2 - 1 - 2s/k_0 - s^2/k_0^2\} + O(s^{2M+1}). \tag{39}$$

Replacing γ in the above analysis with γ_M in Eq. (39) yields the same expression for R in both Eq. (32) and Eq. (36).

Comprehensive analytical and graphical results for the reflection coefficient as a function of angle for both absorbing and impedance-matched boundary layers are presented elsewhere.[37] A key finding of this reference is that for a physical absorber the discretization-induced reflection loss from an inhomogeneous layer defined by $\alpha(z_l) \equiv \Im N(z_l)/n(z_l)$ at grid positions $z_l = z_b + l\Delta z$, $\Delta z = h/L$ for $l = 0, \ldots, L$, is given to the first nontrivial order in the grid point spacing by

$$|R| \approx \exp\left[-2\Delta z \sum_{l=0}^{L} \Im\gamma(z_l)\right]. \tag{40}$$

In comparison, for an impedance-matched layer, a z-dependent imaginary stretching of the grid point spacing is obtained by setting the complex distance between grid points z_l and z_{l+1} to

$$\Delta z_l^* = [1 + ia(z_l)]\Delta z, \tag{41}$$

which generates the continuous reflection loss

$$|R| = \exp\left\{-2\Delta z \sum_{l=0}^{L} [a(z_l)\Re\gamma(z_l) + \Im\gamma(z_l)]\right\}. \tag{42}$$

As noted earlier, the discrete nature of the grid points results in additional contributions to the reflection coefficient of Eq. (40) and Eq. (42). For a perfectly matched layer, the discrete reflection coefficient can be shown to be[37]

$$R(z_l) = \tfrac{1}{16}(2i + a_{l-1} + a_{l+1})(a_{l-1} - a_{l+1})\Gamma^2 + O(\Gamma^4), \tag{43}$$

where $\Gamma^2 = 2 - 2\cos(\gamma\Delta z)$ and we have set $a_l = a(z_l)$. Defining a "mathematically equivalent" lossy absorber defined by the requirement that the transverse decay of a plane wave in an isotropic PML medium equals that of an impedance-matched layer with a specified $a(z_l) \equiv H_l(p,q)$, we find that the extra reflection to Eq. (40) attributed to the discrete grid point spacing is

$$R(z_l) = \frac{a_l - a_{l+1}}{2i + a_l + a_{l+1}} + O(\Gamma). \tag{44}$$

Since Eq. (43) is second-order rather than zero-order in Γ, the discretization-induced reflection for the perfectly matched layer is typically several orders of magnitude smaller than that associated with a physical absorber.

Finally, we remark that to implement the above z-dependent stretching of the imaginary part of the z-coordinate, the finite-difference approximation to the La-

placian operator is constructed from the standard three-point expression for non-equidistant grid points z_{l-1}^*, z_l^*, and z_{l+1}^*, namely,

$$\left.\frac{\partial^2\psi}{\partial z^{*2}}\right|_{z=z_l} \approx \frac{2/\Delta z^2}{2+ia_l+ia_{l+1}}\left\{\frac{\psi_{l+1}-\psi_l}{1+ia_{l+1}}-\frac{\psi_l-\psi_{l-1}}{1+ia_l}\right\}. \tag{45}$$

Pressure-release boundary conditions can be applied at the computational window boundary since, for sufficiently large a_l, the overall reflection from an impedance-matched layer is nearly independent of the boundary condition at the layer endpoint except at nearly grazing incidence.[41]

III. NUMERICAL RESULTS

Three test cases were chosen to examine the degree to which a numerical implementation of the impedance-matched absorbing boundary condition eliminates reflections from the edges of the computational domain. The first case involves the reflection of a Gaussian acoustic beam that is steered obliquely toward an impedance-matched layer. This case is intended to establish the degree to which the reflection coefficient depends on the type of propagator employed. The second case involves a modified Lloyd mirror configuration adapted from PE Workshop II Test Case 1[2] and is designed to study the ability of the impedance-matched layer (IML) to absorb highly divergent radiation from a point source. Finally, in the third case, a leaky waveguide configuration (Ref. 1, pp. 249–251) due to Bucker is used to compare the effectiveness of the impedance-matched layer with that of previous methods based on the use of absorbing layers and nonlocal boundary conditions.[15,19]

A. Example 1: Gaussian beam

The field of a single-frequency acoustic Gaussian beam has a z-dependent profile at $r=0$ in the form ($w=30$ m)

$$\psi(z)=\exp[-(z-z_0)^2/w^2+ik_0\sin\theta z)]. \tag{46}$$

Specifically, we consider a 40-Hz beam steered downwards at an angle of $\theta=45°$ with respect to the pressure-release ocean surface along $z=0$. The medium in $z>0$ is taken to be lossless with a uniform sound speed and density of 1500 m s^{-1} and 1 g cm^{-3}, respectively. The beam is propagated downrange on a computational mesh of range step $\Delta r=10$ m and depth step $\Delta z=4$ m and is allowed to interact with an impedance-matched boundary layer that occupies the region $840<z<1000$ m. For the purpose of this test case, the 40-point PML is parameterized by $H_l(4,1)$ in Eq. (37). Numerical experience indicates that a considerably thinner absorbing region could be employed subject to a careful optimization of the layer properties.

For each calculation, the operator X is first constructed by discretizing the appropriate approximations to Eq. (3), together with the impedance-matched or absorbing boundary conditions on the 250-point transverse spatial grid. Subsequently, each relevant propagator, Eqs. (4), (7), (8) or (17), is evaluated numerically by performing the indicated matrix inversions, multiplications, square-root operations and/or exponentiations exactly as specified in the relevant expression. The resulting matrix representation of the propagator is then applied to advance the initial acoustic field in Eq. (46) through repeated matrix-vector multiplications. For example, the acoustic field amplitude profile at $r=500$ m, calculated with a [4,4]-Padé approximation to the square-root function using this technique, is displayed in Fig. 1. The propagated field (solid line) at the lower computational window boundary is observed to be negligible in accordance with Eq. (42). Therefore, the reflection from the boundary layer is dominated by the reflectivity induced by the discrete grid, except for very small transverse wave vector components. In contrast, the non-negligible incident field (dashed line) at the upper window boundary persists downrange due to the interaction with the pressure-release surface.

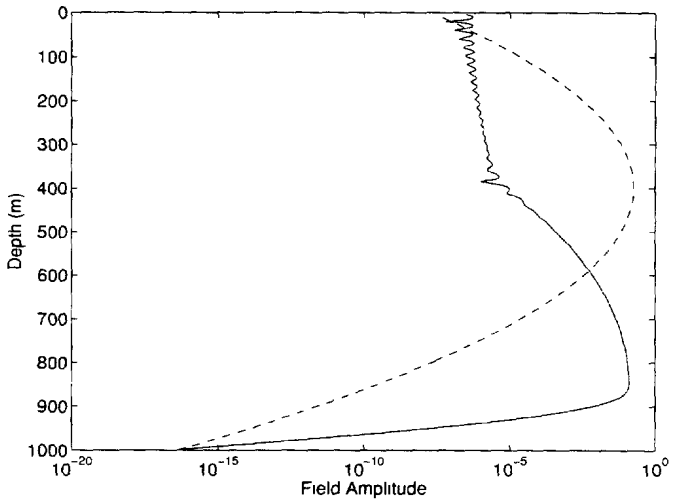

FIG 1 Amplitude of the acoustic field at a range $r=500$ m (solid line) from the Gaussian source field incident at $r=0$ m (dashed line)

In Fig. 2, we display for the exact propagator the power loss $P(r)$ of the propagating field as a function of range, defined as

$$P(r)=-10\log_{10}\frac{\int|\psi(r,z)|^2dz}{\int|\psi(0,z)|^2dz}. \tag{47}$$

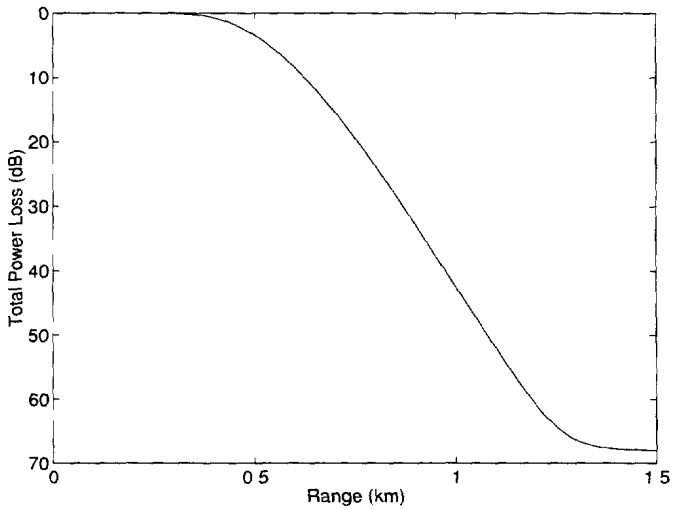

FIG 2 Total field amplitude as a function of range for the Gaussian beam

TABLE I Relative field amplitude of a Gaussian beam after a single reflection from an impedance-matched layer.

Propagator	Total field amplitude
Paraxial	$3\,977\,34\times10^{-4}$
Eq (17), $M=2$	$3\,981\,19\times10^{-4}$
Eq (17), $M=3$	$3.960\,38\times10^{-4}$
Eq (8), $M=2$	$3\,967\,05\times10^{-4}$
Eq (8), $M=4$	$3\,959\,55\times10^{-4}$
Eq (8), $M=8$	$3\,959\,46\times10^{-4}$
Exact propagator	$3\,959\,46\times10^{-4}$

Accounting for the effects of the Gaussian field shape, this curve clearly demonstrates that the field amplitude falls exponentially once the beam is in contact with the impedance-matched boundary layer and then stabilizes after it has fully reflected away from the boundary. The value of the field amplitude after a full reflection from the boundary, which occurs near $r=1500$ m for the exact propagator, provides a convenient measure of the effectiveness of the impedance-matched layer for a given acoustic propagator. This full reflection distance increases to $r\approx1700$ m for the paraxial and low-order Padé propagator approximations since the effective propagation angle that results when these propagators are applied is less than the true 45° beam angle.

In Table I, the relative amplitude calculated after a full reflection (at $r=r'$), namely

$$\exp\{-P(r')/20\}\equiv\left(\frac{\int|\psi(r',z)|^2dz}{\int|\psi(0,z)|^2dz}\right)^{1/2}, \tag{48}$$

is listed for various acoustic propagators. These values are within 1% of each other, and indicate that the magnitude of the reflectivity from the impedance-matched layer, Eq. (42), is comparable for both paraxial and wide-angle methods. Moreover, varying the total propagation distance by ±100 m also changes the predicted loss by less than 1%. We are therefore justified in applying the impedance-matched procedure to realistic wide-angle acoustic calculations in the following section.

B. Example 2: Lloyd mirror

In this example, we consider a fluid medium with the same properties as in the previous example, but with the Gaussian beam source replaced by a 40-Hz point acoustic source located at a depth $z_0=150$ m. The exact solution to this Lloyd mirror problem is given analytically by

$$\psi(r,z)=\sqrt{r}\exp(-ik_0r)\left\{\frac{\exp(ik_0R_-)}{R_-}-\frac{\exp(ik_0R_+)}{R_+}\right\}, \tag{49}$$

where the slant ranges to a receiver from the source and its geometric image about the plane $z=0$ are defined by $R_\pm^2=r^2+(z\pm z_0)^2$. All computations were performed using a 10-m range step, a 0.5-m transverse depth step and a 500-m thick transverse computational domain. To reduce sampling issues associated with the field divergence at the source position, the analytic field in Eq. (49) at a range of 25 m from the source was used to initialize the input acoustic field. The calculation further incorporates a 20-point impedance-matched boundary layer parameterized by $H_l(10,1)$ in Eq. (37).

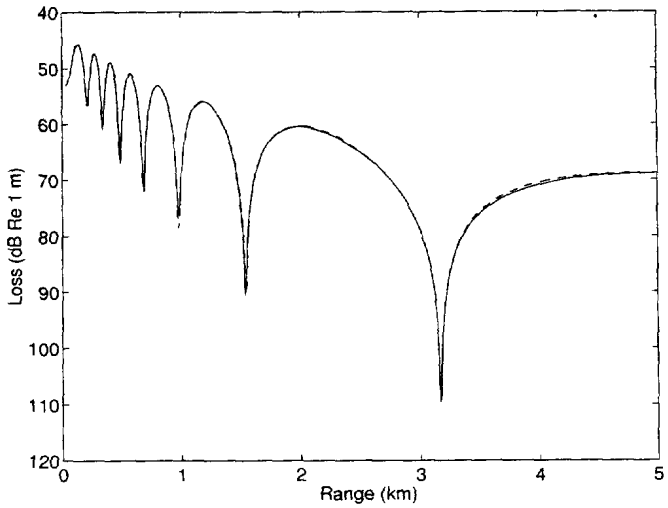

FIG 3 Finite-difference PE transmission loss versus range curves for the Lloyd mirror test case and the exact PE propagator Solid line—analytic calculation Dashed line—calculation with the exact propagator and the impedance-matched layer

In Figs. 3–6, the computed transmission losses $[-10\log_{10}|p(r,z)|^2]$ versus range to a receiver at a depth of $z=400$ m are shown for several propagators together with the known analytic solution given by Eq. (49) (solid line). The dashed line in each figure corresponds to the result obtained using a selected propagator. In particular, the dashed line in Fig. 3 shows the result obtained using the exact propagation formula Eq. (4). Similarly, the dashed lines in Fig 4 and Fig. 5 correspond, respectively, to the $M=1$ and $M=3$ propagators defined by Eq. (8). In the limit of small δ, the $M=1$ propagator approaches the result of the Crank-Nicolson form of the third-order Claerbout equation, Eq. (14). Finally, in Fig. 6, the dashed line corresponds to the [15,15]-Padé approximant with respect to X to the full

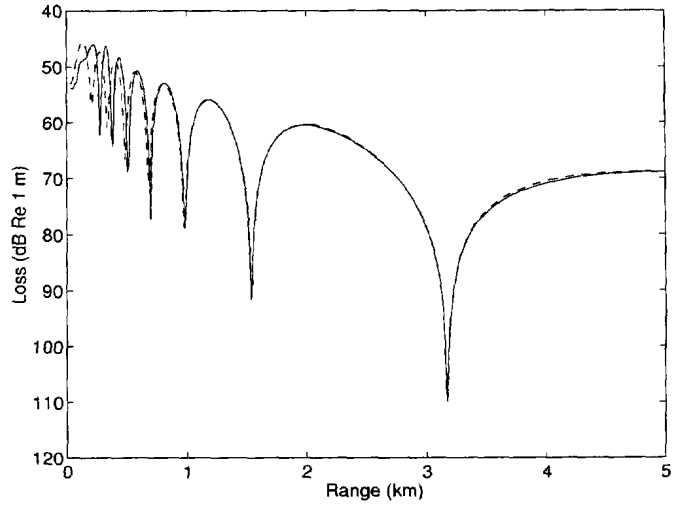

FIG 4 Finite-difference PE transmission loss versus range curves for the Lloyd mirror test case and a propagator based on a [1,1] Padé square-root approximation Solid line—analytic calculation Dashed line—calculation with the approximate propagator and the impedance-matched layer.

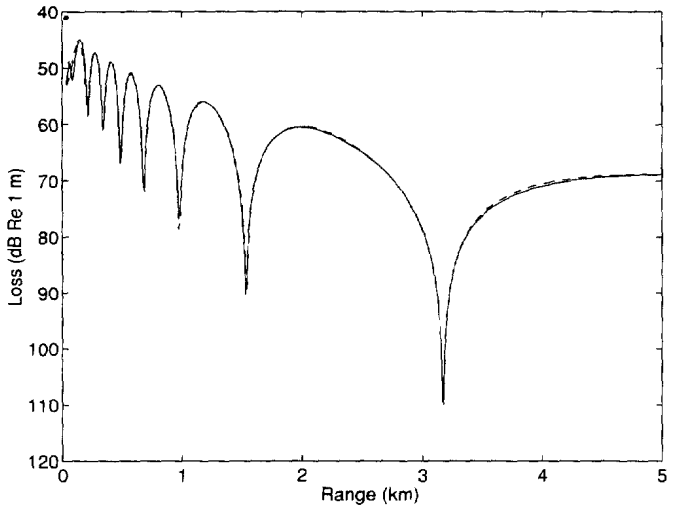

FIG 5 Finite-difference PE transmission loss versus range curves for the Lloyd mirror test case and a propagator based on a [3,3]-Padé approximant to the full propagator Solid line—analytic calculation Dashed line—calculation with the approximate propagator and the impedance-matched layer

propagation operator given by Eq. (15). For all propagators, the results shown are highly insensitive to the strength or width of the impedance-matched layer.

Beginning with Fig. 3, we observe that a slight difference exists in the calculated loss (<0.5 dB) at large ranges between the analytical result and the result obtained using the numerical implementation of the exact propagator. This effect is a result of the finite transverse grid point spacing used in the numerical work, and is therefore common to all of the calculations for the Lloyd mirror example. Next, Fig. 4 clearly demonstrates the wide-angle nature of our calculation, as the exact and Claerbout curves do not agree until the lower-angle energy is dominant beyond a distance of ≈ 1 km. The reduction of the error associated with the wide-angle components of the field afforded by the [3,3]-Padé approximant to the full exponential operator is evident from

TABLE II. Geoacoustic profile for the Bucker example.

Depth (m)	Sound speed ($m\,s^{-1}$)	Density ($g\,cm^{-3}$)	Attenuation dB λ^{-1}
0	1500	1.0	0 0
120	1498	1 0	0 0
240	1500	1.0	0 0
>240	1505	2 1	0 0

the calculated loss curve of Fig. 5, which agrees with the analytic result except for a small region within 100 m of the initial field position. Finally, even this residual error is eliminated by use of the $M=15$ Padé approximation to the square-root operator, which almost precisely coincides with the exact result as shown in Fig. 6. From the excellent agreement between the analytic and numerical curves, we conclude that impedance-matched layers can be employed to absorb the radiation field in wide-angle calculations without degrading the calculational accuracy of the underlying computational algorithm.

C. Example 3: Bucker profile

Finally, we examine the leaky waveguide example given in Table II which is a shallow water problem originally studied by H. Bucker (Ref. 1, pp. 249–251). In the water column, the geoacoustic parameters vary linearly between points. Both sound speed and density undergo jump discontinuities along the ocean bottom. The lossless region $z>240$ m has a uniform sound speed and density of 1505 $m\,s^{-1}$ and 2.1 $g\,cm^{-3}$, respectively. This example has been used previously to examine the effectiveness of absorbing boundary conditions.[15,19]

The transmission loss versus range curves are shown in Fig. 7 for a 100-Hz acoustic source located at $z=30$ m and a receiver depth of $z=90$ m. The solid line in this figure was obtained using the spectral integration model SAFARI.[42] The two other curves were computed using the Claerbout PE in

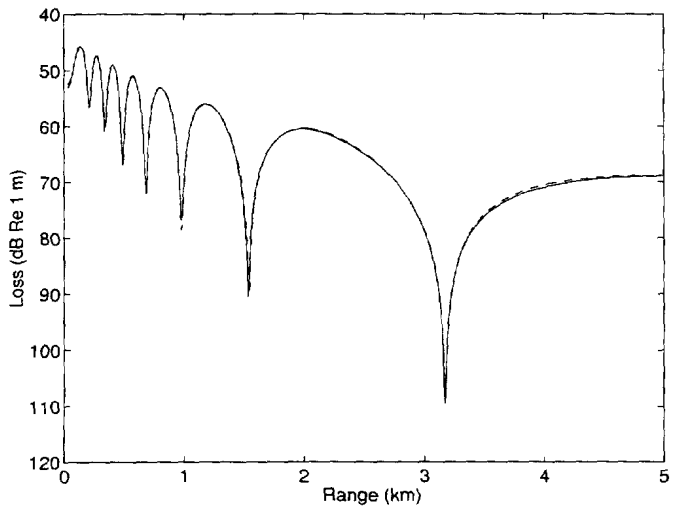

FIG 6 Finite-difference PE transmission loss versus range curves for the Lloyd mirror test case and a propagator based on a [15,15]-Padé square-root approximation Solid line—analytic calculation Dashed line—calculation with the approximate propagator and the impedance-matched layer

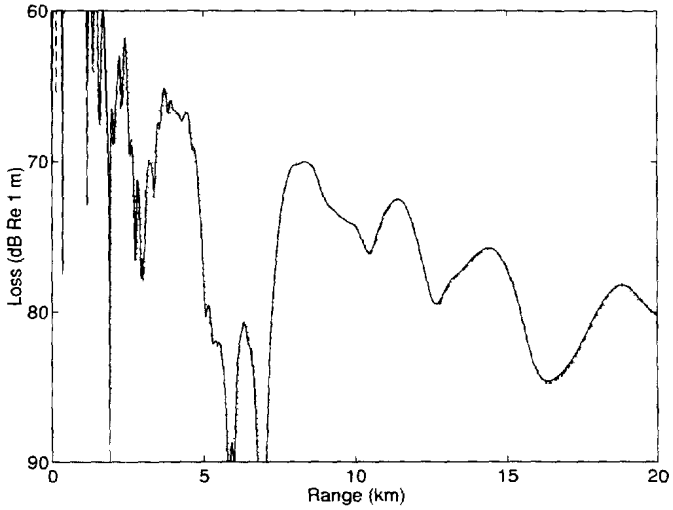

FIG 7 Finite-difference PE transmission loss versus range curves for the Bucker profile Solid line—Claerbout PE calculation with the nonlocal boundary condition Dashed line—SAFARI Dotted line—Claerbout PE with the impedance-matched layer

conjunction with an impedance-matched boundary layer (dotted line) as well as the exact, nonlocal boundary condition (NLBC, dashed line) presented in Ref. 19. The 20-point impedance-matched layer in the region $260<z<300$ m is given by $a_l=H_l(10,2)$ in Eq. (37) while the NLBC was applied at a depth of $z=250$ m (10 m below the sea-bottom interface). Both PE calculations used a range step size of $\Delta r=10$ m, a depth step size of $\Delta z=2$ m, and a value of $c_0=1500\ \mathrm{m\,s^{-1}}$ for the reference sound speed.

The excellent agreement between the computed impedance-matched layer transmission losses and the SAFARI and PE+NLBC results demonstrates the practical efficiency of this method. The small discrepancies at long range are attributable to discretization-induced reflection, as explained above, as well as to numerical errors in the excitation field arising from the finite number of grid points, as we have verified by repeating our impedance-matched calculation with different window widths. (In fact, the latter effects were previously observed in calculations using the Papadakis nonlocal boundary conditions.) Although as before, the layer strength and width have not been optimized, our results compare favorably with those obtained using a traditional linearly increasing absorber, which requires a typical thickness of 500–1000 m to achieve equivalent accuracy.

IV. CONCLUSIONS

In this paper, we have demonstrated that an impedance-matched layer can be constructed for both paraxial and wide-angle acoustic wave propagation that yields a highly efficient procedure for absorbing radiating fields at the computational boundary. In particular, we first considered the reflection of a Gaussian beam from an impedance-matched boundary and found that the computed reflection coefficient is nearly independent of the angular accuracy of the underlying propagator. We further examined two standard acoustic test problems using different paraxial and wide-angle propagators. In all cases the results agreed very well with exact results even for very thin impedance-matched layer regions. Use of a traditional absorbing layer typically requires far more grid points in these cases to achieve a similar level of accuracy. Accordingly, we conclude that while transparent boundary conditions such as those of Refs. 14, 15, and 19 are optimal for two-dimensional near-paraxial propagation problems that can be modeled with either the Fresnel or Claerbout equations, the impedance-matched condition investigated above can be applied to two-dimensional wide-angle as well as paraxial and wide-angle three-dimensional problems for which accurate and convenient nonlocal boundary conditions remain to be formulated.

[1] F B Jensen, W. A. Kuperman, M B Porter, and H Schmidt, *Computational Ocean Acoustics* (AIP, New York, 1994)

[2] M D Collins, "Higher-order, energy-conserving, two-way, and elastic parabolic equations," in *PE Workshop II Proceedings of the Second Parabolic Equation Workshop*, edited by S. A Chin-Bing, D B. King, J A Davis, and R. B Evans (Naval Research Laboratory, U S Government Printing Office, 1993), pp 145–168

[3] J. R. Kuttler and G. D. Dockery, "Theoretical description of the parabolic approximation/Fourier split-step method of representing electromagnetic propagation in the troposphere," Radio Sci. **26**, 381–393 (1991)

[4] K E Gilbert and X Di, "A fast Green's function method for one-way sound propagation in the atmosphere," J. Acoust. Soc. Am **94**, 2343–2352 (1993)

[5] J S Papadakis, M I Taroudakis, P J. Papadakis, and B Mayfield, "A new method for a realistic treatment of the sea bottom in the parabolic approximation," J Acoust Soc. Am **92**, 2030–2038 (1992).

[6] S M Flatte and F D Tappert, "Calculation of the effect of internal waves on oceanic sound transmission," J Acoust Soc Am **58**, 1151–1159 (1976)

[7] F D Tappert, "The parabolic approximation method," in *Wave Propagation and Underwater Acoustics*, edited by J B Keller and J S Papadakis (Springer, New York, 1977), Chap 5, pp 224–287

[8] J A Davis, D White, and R C Cavanagh, "NORDA Parabolic Equation Workshop, 31 March–3 April 1981," Naval Ocean Research and Development Activity, NSTL Station, MS, Tech. Note 143, 1982.

[9] D. J. Thomson, "Wide-angle parabolic equation solutions to two range-dependent benchmark problems," J Acoust Soc. Am **87**, 1514–1520 (1990).

[10] D Yevick, J Yu, and Y. Yayon, "Optimal absorbing boundary conditions," J Opt Soc Am A **12**, 107–110 (1995)

[11] C Vassallo and F Collino, "Highly efficient absorbing boundary conditions for the beam propagation method," J Lightwave Technol **14**, 1570–1577 (1996).

[12] D. T Prescott and N V Shuley, "Reflection analysis of FDTD boundary conditions—Part I Time-space absorbing boundaries," IEEE Trans Microwave Theory Tech **45**, 1162–1170 (1997).

[13] S W Marcus, "A hybrid (finite-difference–surface Green's function) method for computing transmission losses in an inhomogeneous atmosphere over irregular terrain," IEEE Trans. Antennas Propag **40**, 1451–1458 (1992)

[14] J S. Papadakis, "Exact, nonreflecting boundary conditions for parabolic-type approximations in underwater acoustics," J Comput. Acoust **2**, 83–98 (1994)

[15] D J Thomson and M E. Mayfield, "An exact radiation condition for use with the *a posteriori* PE method," J Comput Acoust. **2**, 113–132 (1994)

[16] F Schmidt and P Deuflhard, "Discrete transparent boundary condition for the numerical solution of Fresnel's equation," Comput. Math Appl **29**, 53–76 (1995)

[17] A V Popov, "Accurate modeling of transparent boundaries in quasi-optics," Radio Sci. **31**, 1781–1790 (1996)

[18] M F Levy, "Transparent boundary conditions for parabolic equation solutions of radiowave propagation problems," IEEE Trans Antennas Propag **45**, 66–72 (1997).

[19] D Yevick and D J Thomson, "Nonlocal boundary conditions for finite-difference parabolic equation solvers," J Acoust Soc Am **106**, 143–150 (1999)

[20] F Schmidt and D. Yevick, "Analysis of boundary conditions for the Fresnel equation," J Comput Phys **134**, 96–107 (1997)

[21] M. D Collins, "Benchmark calculations for higher-order parabolic equations," J Acoust Soc Am **87**, 1535–1538 (1990)

[22] M D Collins, "A split-step Padé solution for the parabolic equation method," J Acoust Soc Am **93**, 1736–1742 (1993).

[23] V Shevshenko, "The expansion of the fields of open waveguides in proper and improper modes," Radiophys Quantum Electron **14**, 972–977 (1974)

[24] J.-P Bérenger, "A perfectly matched layer for the absorption of electromagnetic waves," J Comput Phys **114**, 185–200 (1994)

[25] D Katz, E Thiele, and A Taflove, "Validation and extension to three dimensions of the Berénger PML absorbing boundary condition for FD-TD meshes," IEEE Microwave Guid Wave Lett **4**, 268–270 (1994)

[26] W C Chew and W H Weedon, "A 3D perfectly matched medium from modified Maxwell's equations with stretched coordinates," Microwave Opt Technol. Lett **7**, 599–604 (1994)

[27] R Mittra and U Pekel, "A new look at the perfectly matched layer (PML) concept for the reflectionless absorption of electromagnetic waves," IEEE Microwave Guid. Wave Lett **5**, 84–86 (1995)

[28] C Rappaport, "Perfectly matched absorbing boundary conditions based on anisotropic lossy maping of space," IEEE Microwave Guid Wave Lett **5**, 90–92 (1995)

[29] B Chen and D G Fang, "Modified Berénger's PML absorbing boundary conditions for FD-TD meshes," IEEE Microwave Guid Wave Lett **5**, 399–401 (1995).

[30] J. Fang and Z Wu, "Generalized perfectly matched layer–An extension of Berénger's perfectly matched layer boundary condition," IEEE Microwave Guid Wave Lett **5**, 451–453 (1995)

[31] Q H. Liu and J. Tao, "The perfectly matched layer for acoustic waves in absorbtive media," J Acoust. Soc Am **102**, 2072–2081 (1997)
[32] D M Sullivan, "An unsplit step 3-D PML for use with the FDTD method," IEEE Microwave Guid. Wave Lett **7**, 184–186 (1997)
[33] J.-P Bérenger, "An effective PML for the absorption of evanescent waves in waveguides," IEEE Microwave Guid Wave Lett **8**, 188–190 (1998)
[34] W.-P Huang, C. L Xu, W. Lui, and K Yokoyama, "The perfectly matched layer boundary condition for modal analysis of optical waveguides: Leaky mode calculations," IEEE Photonics Technol Lett **8**, 652–654 (1996)
[35] W W Lui, K Magari, N Yoshimoto, S Oku, T Hirono, K Yokoyama, and W.-P Huang, "Modeling and design of bending waveguide based semiconductor polarization rotators," IEEE Photonics Technol Lett **9**, 1379–1381 (1997)
[36] W C Chew and Q H Liu, "Perfectly matched layers for elastodynamics A new absorbing boundary condition," J Comput. Acoust. **4**, 72–79 (1996)
[37] D Yevick, J Yu, and F. Schmidt, "Analytic studies of absorbing and impedance-matched boundary layers," IEEE Photonics Technol. Lett. **9**, 73–75 (1997)
[38] F Collino, "Perfectly matched absorbing layers for the paraxial equations," J Comput Phys **131**, 164–180 (1997)
[39] J. F Claerbout, "Coarse grid calculations of waves in inhomogeneous media with application to delineation of complicated seismic structure," Geophysics **35**, 407–418 (1970)
[40] G. H Brooke and D. J Thomson, "Non-local boundary conditions for high-order PE models with application to scattering from a rough surface," Defence Research Establishment Atlantic, Dartmouth, N S., Tech Memo DREA TM 1999–121, August 1999
[41] D T Prescott and N V Shuley, "Reflection analysis of FDTD boundary conditions—Part II: Bérenger's PML absorbing layers," IEEE Trans Microwave Theory Tech **45**, 1171–1178 (1997)
[42] H Schmidt, "SAFARI Seismo-acoustic fast field algorithm for range-independent environments," SACLANT Undersea Research Centre, San Bartolomeo, Italy, Rep SR-113, 1988

#514630